

Seismic hazard in low slip rate crustal faults, estimating the characteristic event and the most hazardous zone: study case San Ramón fault, in central Andes.

Nicolás P. Estay^{1,2}, Gonzalo Yáñez^{1,2,3}, Sebastien Carretier^{4,5,6,7}, Elias Lira¹, José Maringue¹

5 ¹ Pontificia Universidad Católica de Chile, Santiago, Vicuña Mackenna 4686, Chile

² CIGIDEN, Santiago, Vicuña Mackenna 4686, Chile

³ CEGA, Santiago, Vicuña Mackenna 4686, Chile

⁴ IRD, UR 234, GET, 14 avenue E. Belin, F-31400, Toulouse, France

⁵ Université de Toulouse, UPS, GET, 14 avenue E. Belin, F-31400, Toulouse, France

10 ⁶ CNRS, GET, 14 avenue E. Belin, F-31400, Toulouse, France

⁷ Departamento de Geología, FCFM, Universidad de Chile, Beauchef 850, Santiago, Chile

Correspondence to: N. P. Estay (nnperez@puc.cl)

Abstract. Crustal faults located nearby cities may induce catastrophic damages. When recurrence times are in the range of
15 1.000-10.000 or higher, actions to mitigate the effects of the associated earthquake are hampered by the lack of a full seismic
record, and in many cases, also of geological evidences. The San Ramón fault is a ~ 30 km NS trending fault with low slip
rate (0.1 - 0.5 mm yr⁻¹), located at the foothills of the Andes, near a large city Santiago, the capital of Chile (>6.000.000
inhab.). In order to characterize the fault behaviour and its effects, we propose three different already developed time-
integration methodologies to define the most likely scenarios of rupture, and then to quantify the hazard with an empirical
20 equation of peak ground acceleration (PGA). We consider the following methodologies, (1) stream gradient and (2) sinuosity
indexes, to estimate fault-related topographic effects; and (3) gravity profiles across the fault, to identify the fault scarp in the
basement. Along the fault trace we define 4 segments that probably get active independently, with a mean length of ~ 10 km.
We tested the present-day seismic activity by the deployment of a local seismologic network during one year, finding 5
events spatially related to the fault. In addition, fault geometry along the most evident scarp was imaged in terms of its
25 electrical resistivity response by a high resolution TEM (transient electromagnetic) profile. Seismic events distribution and
TEM imaging allowed to constrain the fault dip angle (~ 65°) and its capacity to break into surface. Using the empirical
equation of Chiou & Youngs (2014) for crustal faults and considering the characteristic seismic event (thrust high-angle
fault, ~10 km, Mw 6.2 - 6.7), we estimate the acceleration distribution in Santiago city and the hazardous zones. City
domains are under high risk included the hanging wall zone covered by sediments and narrow zones where the fault could
30 break the surface. Over these domains, horizontal PGA can be greater than 0.5g and eventually producing building collapse.

1 Introduction

In active margins, sustainable balance between city development and geological environment require the understanding of seismic hazard to reduce the associated risks. When cities emplacements are adjacent to potentially active crustal faults, seismic risk are elevated, thus it is important to quantify their possible effects. A good example to demonstrate the potential danger of crustal faults is the Niigata Mw = 6.6 earthquake dated in 2004, Japan. This country has high standards of anti-seismic norms and therefore the expected damage in a given event is low. Nevertheless, 48 deaths and 5000 houses destroyed or with important damage were reported (Scawthorn & Rathje, 2006). Considering only the last decades, several crustal catastrophic events have been reported, affecting human lives and infrastructures. Some examples are the Nepal earthquake Mw = 7.8 on 25 April 2015, with more than 1500 deaths and 10000 wounded; and in the Andes, the Mw = 6.2 earthquake on 26 January 1985 in Mendoza, with 6 deaths and more than 12500 constructions destroyed. The previous account motivates the developing of the best possible knowledge to mitigate the seismic risk associated with crustal faults that are found near highly populated cities. This assessment is relatively simpler when fault rates are high or a large earthquake happens in instrumental or historic times. This is more difficult when none of these conditions are met. An example of this case is the San Ramón fault (SRF) in the central Andes (Fig. 1), located at the foot hills of Santiago city, the highly populated capital of Chile (>6.000.000 inhab) (Armijo et al., 2010; Farías et al., 2008; Rauld et al., 2006; Vargas et al., 2014). We choose this case for the high potential risk associated, and the chances to propose and test an integrated methodology to estimate the seismic hazard.

Defining whether or not the fault is active is crucial to affirm that the risk exists. An active fault which is preferentially oriented with respect to the current tectonic regime allows the stress release, eventually triggering earthquakes (examples of preferentially oriented faults are normal and thrust faults subject to Andersonian regime, with strike perpendicular to σ_3 and sigma σ_1 respectively). Although the lack of seismic events does not necessarily imply fault inactivity, seismic recording could suggest an active condition. In order to identify the potential seismic activity we deployed a micro-seismic network of 5 stations for one year. We acknowledge that a definitive answer at this regard requires decades of seismic recording, however with one year time window we are able to have a first order idea on the fault activity.

Along the SRF, the probable low recurrence of the characteristic earthquakes, 9 ± 0.5 kyrs (Vargas et al. 2014), requires a complementary approach to characterize its geometry and long-term behaviour. One important variable to understand the seismic hazard is the rupture length of a characteristic earthquake. A characteristic earthquake represents a repeating event that accumulates the most important displacement in the fault (Schwartz & Coppersmith, 1984). A good strategy to estimate the rupture length is defining some methodologies capable of integrating the fault displacement on time. Consistent with this strategy, we consider the following methodologies: 1) The stream gradient index, that can compare the relative uplift rate in a certain area, studying the topographic profile of near-fault rivers (e.g. Font et al. 2010; Casa et al. 2010); 2) The sinuosity index that estimates the uplift of a fault observing the sinuosity of the mountain front (Bull & McFadden, 1977); 3) Across-fault gravity profiles to estimate the shape of the fault scarp in the basement beneath the sedimentary basin, given the large

density contrast between rocks and sediments. Basement morphology is a useful marker of cumulative faulting. Since SRF has a low slip rate, fault scarp morphology may be modified by deposit and/or erosion surface processes. Thus, we favour the use of gravity profiles and geomorphological measurements instead of scarp topographic analyses.

As a final product of this research we tackle the difficult question of relating the occurrence of a given seismic event with an associated damage prediction. One possibility is to estimate the expected acceleration during a characteristic earthquake, and then links this output with damage. Acceleration is an objective measure of the seismic effects, and thus it is not affected by the quality of the housing or infrastructure. We choose the empirical equations for crustal earthquakes (e.g. Sadigh et al. 1997; Chiou & Youngs 2014) to predict the peak ground acceleration (PGA). The robustness of this methodology is grounded on the last decade understanding of the key variables that control the PGA. Principal variables are event magnitude, fault type, and hanging wall effects. We choose the Chiou & Young equation (2014), because this model accounts also for a low slip rate crustal fault, and has an extensive record of different earthquakes in the world. In order to use this particular approach, further parameters are required, such as the shallow depth of the rupture and the dip of the fault. We estimated these parameters with a joint interpretation of the surface geology (Armijo et al., 2010; Rauld, 2011; Vargas et al., 2014), the results of the micro-seismic study, and a high resolution 2D geo-electrical TEM study.

15 2 Geological settings

This region is dominated by the subduction of the Nazca plate underneath the South American plate, since at least the Jurassic time (Mpodozis & Ramos, 1989). Upper basement rocks are dominated by the volcano-sedimentary Abanico and Farellones formations. These **volcano-sedimentary sequences are mainly constituted by pyroclastic strata**, interdigitated with lava and different sedimentary rocks. The earliest Abanico formation was deposited during the Late Eocene-Oligocene and has been deformed later on (Charrier et al., 2002; Godoy, Yañez, & Vera, 1999). Farellones formation was deposited above the underlying sequence, during the Early and Middle Miocene (Charrier et al., 2002). These volcano-sedimentary sequences are also intruded by Miocene plutons (Kurtz, Kay, Charrier, & Farrar, 1997; Thiele, 1980). Among them, we find La Obra pluton 19.6 ± 0.5 Ma (Kurtz et al., 1997), emplaced at the foot hills of the Andes near the SRF (Thiele 1980).

The Santiago basin sediments can be grouped into three main sequences. The wide-spread and well compacted fluvial sediments, associated with the material transport along the Maipo and Mapocho rivers (i.e. Leyton, 2010; Yañez et al., 2015). In addition there are the alluvial and coluvial deposits, which are semi-compacted and spatially concentrate at the piedmont of the Andes (Fernández, 2003). Finally, and restricted to the northern area of the study, it is possible to find fine soil, mostly lacustrine deposits, **and to a lesser extent, pyroclastic ash** related to the Maipo volcano eruption ~450.000 years ago (Stern et al., 1984).

The San Ramón fault has been studied using high resolution DEM, satellites images, and field observations (Armijo et al., 2010; Rauld, 2011). These authors conclude that the SRF is a west-verging reverse fault that accommodates the compressive stress regime in this segment of the central Andes (see Fig. 1). One of the best outcrops to observe the fault can be examined

in Fig. 4c. The ignimbrite of Maipo eruption ~450.000 years ago, allows a rough estimation of fault slip rate considering that these deposits are preserved in the hanging and foot wall. The offset of 60 m determines a minimum slip rate of 0.13 mm per year (Armijo et al., 2010). A paleo-seismological study in one trench (Vargas et al. 2014) identifies 2 events in the last 17-19 kyrs, with a cumulative displacement of 9.7 ± 1.2 m, considering the fold of the layers. The mean slip rate of the two events is $0.45\text{-}0.64$ mm yr⁻¹, with a recurrence time of 9 ± 0.5 kyrs for characteristic earthquakes. A maximum earthquake magnitude has been discussed, in a range of 6.3-7.5 Mw (Armijo et al., 2010; Pérez et al., 2014; Rauld, 2011; Vargas et al., 2014). Differences in the magnitude estimated are a function of the number of fault segments that might be activated synchronically, and the fault width. If the segments ($\sim 15 \times 15$ km²) get active independently can generate a 6.6-7.0 Mw earthquake, while the simultaneous activation of all segments (listric fault of 30×30 km²) would produce a seismic event of 6.9-7.4 Mw (Armijo et al., 2010). **Until now, the seismic hazard analysis has only considered this worse-case-scenario (Pérez et al., 2014), neglecting the likelihood of other intermediate options.** At this regard, we focus this work on a better definition of the SRF fault segmentation, minimizing the smoothing effect of erosion and deposit processes, providing in this way new insights on the most likely characteristic earthquake length.

3 Methodology

15 In order to get an estimate of the seismic hazard on SRF, we consider five steps (see flow chart in Fig. 2). In this chapter we describe briefly these methodological steps, and in chapter 4 we present the results derived from their application.

3.1 Present-day fault activity

To achieve the first goal, we deployed a small seismic network of five borehole seismometers with three-component 2 Hz sensors running in continuous mode with a sample rate of 100 Hz. The equipments were installed near the fault trace; covering an area of $20\text{km} \times 15\text{km}$ (see Fig. 3). The preliminary estimate of the origin times and hypocentral coordinates was determined by means of the HYPOINVERSE program (Klein, 1978), considering the initial velocity model proposed by Villegas (2012) for this area. Then we made a recursive process for the best estimate of velocity structure and event location, using the VELEST and HYPOINVERSE code (Kissling et al. 1994). The model with the lowest RMS error has 10 layers and assumes a varying Vp/Vs ratio. The best model was reached after 7 iterations.

25 The association of seismic events and SRF is determined by the following procedure. Given the SRF surface trace we project its potential extension downwards (Wells & Coppersmith, 1994). **Well localized events which are located inside the area of fault influence are considered a likely representation of fault activity.** These events were projected into a central cross-section perpendicular to the fault, for visual discrimination of truly fault-related events. Comparing the amount of events related to the fault, **with those from other structures**, it can be discussed the importance of the fault in the stress release of the whole zone.

3.2 Fault geometry, dip and depth of rupture

To determine the geometrical characteristics of the fault, we consider the available data on the literature (Armijo et al. 2010; Vargas et al. 2014), the spatial distribution of seismic events, and a 2D resistivity image on a well maintained scarp. The electrical imaging was obtained by carrying out a high resolution TEM (Transient Electro Magnetic) experiment that provides a good constraint for the first 150-200 m fault section. TEM technique is a geophysical method which allows to get an electrical resistivity image of the subsurface (for details of TEM theory and data processing see for instance Telford et al. 1990). In the field, we used the FastSnap System, completing 24 TEM stations separated by 25 m from each other. For the purpose of getting the maximum spatial resolution we use the in-loop configuration with a transmitter (Tx) loop of $25 \times 25 \text{ m}^2$ with 1 and 4 turns, and a central receiver loop (Rx) $5 \times 5 \text{ m}$. The receiving coil records the voltage decay for 100 pulses at different sampling rates (frequencies). A stacking for each frequency is performed to reduce noise. Following this procedure a final voltage decay curve versus time is generated, and then modeled and inverted. The inversion is made through iteration of different resistivity/depth models (assuming flat layers) to converge to a solution with an acceptable error (less than 5%). The process and the modeling were done with the FastSnap computer software (TEM -Processing 1.1 Model 3.0). A 2-D pseudo depth-section is obtained gridding the 1-D inversions of each TEM station. This electrical image provides an estimate of the near-surface fault geometry.

3.3 Rupture length and M_w of the characteristic earthquake

An empirical first-order relationship between rupture length and earthquake size (Blaser et al., 2010; Wells & Coppersmith, 1994), allows the estimate of the characteristic earthquake magnitude based on a well constrained rupture length. In this case we use three different methodologies to quantify this length in terms of the associated uplift. Each independent methodology estimates the fault uplift, measuring physical or geomorphologic properties. These methodologies are:

1) Across-strike gravimetric profiles. Due to the low erosion rate of the basement, tectonic deformation is better preserved in basement compared to the surface. **Density contrast between gravel material and basement rocks** makes the gravity method a suitable tool to estimate basement geometry across the fault. We did 24 gravity profiles across the SRF, with lengths of 2-3 km. We used sampling distance of 100 m (in the fault core) and 200 m (at the flanks), and distance between profiles of 3-8 km (see profiles location in Fig. 6). We used the software Model Vision for the 2.5D gravity forward modeling. This modeling effort involves the estimate of a second order regional field to account for the basement heterogeneities, and the modeling of the mass-deficiency residual gravity field (for details of the gravity methods and data reduction/modeling see Telford et al., 1990).

2) **Stream Gradient Index**. This index represents a relative measure of the surface uplift based on drain topographic profiles (Hack, 1973; Merritts & Vincent, 1989). Zones with high values suggest larger surface uplift relative to zones with low values (e.g. Casa et al., 2010; Font et al., 2010). This methodology is useful because drainage profiles are good indicators of the long term uplift process. To determine the corresponding drainage, we used the Arcgis utilities flow direction, flow

accumulation and watershed. We only chose secondary drainage with similar length, to avoid potential bias associated with different scale processes. To calculate the Stream gradient index (hereafter SL) we separate the topographic profiles of each drainage into several segments with 50 meters of elevation overlap. For each segment, SL was calculated multiplying the slope by the middle distance to the drain top (Hack, 1973; Merritts & Vincent, 1989).

- 5 3) Sinuosity Index. Long-term activity of a piedmont fault can be inferred from mountain front sinuosity index (Bull & McFadden, 1977). Low values of this index indicate a fault-controlled landscape (Bull & McFadden, 1977), and the minimum value is 1.00. This index was developed for normal faults, but it has been satisfactorily proven in reverse faults (Casa et al., 2010; Jain & Verma, 2006; Singh & Tandon, 2007; Wells et al., 1988). At the transition between mountain front (high slope) and basin (low slope), across-strike slope differences generate an anomaly angle. We used Arcgis to generate a slope map, and define the best slope angle that represents the basement-basin contact, comparing the slope map with the most detailed geology information (in this case Rauld, 2011). In the present study, this angle is between 15° and 16°. We separated the fault into different segments where the basement-basin contact shows a constant sinuosity. Then, the fault length for each segment was calculated by the geological surface identification available (Armijo et al., 2010). **In zones where the fault has not been previously mapped, we propose a straight trace parallel to the mountain front.**
- 10
- 15 Results from each methodology will be discussed separately, and then a joint interpretation will be made to define the rupture length of the characteristic earthquake.

3.4 PGA field associated to the characteristic earthquake

Based on the length of characteristic earthquake rupture and fault geometry, we estimate the seismic hazard by calculating the corresponding peak ground acceleration (PGA). In this work we used the attenuation model of Chiou & Youngs (2014), appropriate for crustal earthquakes. PGA field is calculated over a grid of one kilometer spacing. Each grid point is characterized by the associated basement depth and weighted average shear wave velocity for the first 30 meters (V_{s30}), both first-order parameters to quantify site effects. We use the basement depth defined by Yañez et al. (2015), while the shear wave velocity is taken from the basin seismic micro-zonation of Leyton et al. (2010). Finally, PGA estimate for each grid point corresponds to the maximum PGA among all probable rupture scenarios.

25 3.5 SRF Seismic hazard in Santiago City vs. Subduction events

The hazardous domains derived from the PGA maps are defined in terms of the acceleration distribution. In order to gain some insight on the effects of an SRF event, we compared the expected acceleration estimated in this study with the observed acceleration during the Maule 2010 Mw=8.8 earthquake. Assuming that the observed damages are directly related to the PGA, and with minor influence to other variables like the time-length of earthquake, this comparison provides a simple mechanism to estimate the expected damage for an SRF characteristic earthquake.

- 30

4. Results

4.1 Present-day fault activity (Seismic study)

Over the year of micro-seismic recording we identified 1666 events within a radius of 150 km around the network. The majority are located on the Nazca-South American plate contact, and only 245 of them are crustal intraplate earthquakes with depth above 35km. Fifty-six percent of these crustal earthquakes are related to blasts in mining operations, and only the remaining 44% (110 events) are associated with natural sources. Some events were well registered in only two stations, implying large position errors. To have certainty on earthquake locations, we restricted the position errors to eight kilometers, in both horizontal and vertical coordinates. Well recorded crustal events are constrained to an 80×100 km area. The horizontal projection of these seismic events is presented in Fig. 3. We include in this figure two areas that simulate the horizontal projection of two likely fault planes, 30° and 70° . The associated widths were defined by empirical geometrical relationships (Wells & Coppersmith, 1994). In the same figure we include a depth cross-section where all the seismic events inside these areas are projected. Some seismic events are associated with a hypothetical high angle fault (60 - 65° dip, 5 events), whereas the low angle fault scenario (30° dip) does not fit with the observed seismicity depth distribution.

4.2 Fault geometry, dip and depth of rupture (TEM)

The resistivity imaging (Fig. 4) reveals different domains below the well-preserved scarp. Electrical domains are sub-horizontal in the first 100-150 m depth and homogeneous at both edges. But in the fault core, electrical domains are clearly sub-vertical below 100-150 m depth. We associate the relative conducting and sub-horizontal upper domain with the sedimentary infill of the basin at the foot hills. Below the sedimentary cover we associated the electrical high or low resistivity domains with pristine or fracture basement rocks respectively. Consistent with this observation, it is possible to separate the electrical image in six different units (see Fig. 4b). I) Quaternary high resistivity sediments at the colluvial wedge of the scarp (mean resistivity 144 ohm-m). II) Quaternary relatively dry sediments (45 ohm-m). III) Upstream quaternary wet sediments in the fault hanging wall (25 ohm-m). IV) Pristine basement rock (+1000 ohm-m). V) Low resistivity domain, associated with fluid percolation along fractured rocks (1.6 ohm-m). In some cases, the resistivity is less than 1 ohm-m, probably due to the presence of highly saline hydrothermal fluids that uses fault planes as conduits. VI) Unconsolidated sediments interbedded with hydrothermal fluids downstream with respect to the fault (0.5 ohm-m).

In terms of the fault geometry, this geoelectrical imaging represents a family of nearly vertical low/high resistivity bodies, interpreted as a system of high angle faults reaching the surface.

4.3 Gravity profile

Gravity modeling demonstrates that cumulative deformation is better expressed in the basement. This behavior is confirmed in the inversion of gravity profiles that cross an evident fault scarp (e.g. Profile 7 in Fig. 5). The surface scarp observed in the elevation profile (Fig. 5), is less abrupt than the basement scarp observed in the gravity inversion. Basement scarps are

characterized by short wavelength (<200 m) and relatively large size (>10 m) gravity bodies. In addition, the gravity inversion of profile 7 identifies 3 scarps in basement whereas only two appear at the surface. The erosion process smooths the surface diluting the presence of multiple scarps, either by the retreat of previous scarp, or as an effect of diffusive erosion (e.g. Carretier et al. 2002).

5 To understand the along-strike continuity of the basement scarp, and thus the possible rupture length, we mapped all the identified basement scarps. One example of this scarp continuity analysis is shown in Fig. 5. In this case we can observe several scarps in N-S strike continuity. Another important measure obtained in the gravity inversion is the accumulated displacement on each profile, a complementary approach to estimate the rupture continuity (see Fig. 6). The accumulated displacement is estimated by the sum of all the basement scarp-heights at each profile. Both approaches consistently show
10 scarp discontinuities. Based on this observation we define 4 different segments with mean length of 10 km.

4. 4 Stream gradient index (SL)

The SL only holds for long wavelength of the topography, with a cutoff that depends on the available stream network, in this particular case much wider than the gravity approach. The SL results allow the definition of four main domains (see Fig. 7) from north to south. The northern one has a concentration of high SL values, with a NS high anomaly (~5 km length) that
15 cuts two drains. The next zone southwards shows low SL values, in addition with the lack of surface fault manifestation. Further south, in the central area where the SRF has been mapped (Armijo et al., 2010; Rauld, 2011), we find a concentration of high SL values, consistent with the topographic fault expression. This high SL values area has a NS continuity of approximately ~30 km. Finally, at the southern edge we find low SL values coherent with the until now inexistent fault expression found.

20 Lithological differences under the drainage can generate misinterpretation of the SL index as directly bedrock uplift indicator. Considering that intrusive rocks are less erodable than volcanic rocks ($k_{int} < k_{volc}$) (Moore et al., 2009; Stock & Montgomery, 1999), the same tectonic uplift in both units would produce a larger surface uplift in intrusive rocks, given their less erodable condition. In the study area intrusive outcrops show the lowest SL values, evidencing a low surface uplift. This observation validates the use of the SL marker as an estimate of the bedrock uplift, regardless of the lithology in this
25 particular case. To validate our results, we contrast the SL estimate with respect to the approximated erosion rates. Figure 7 shows an approximate erosion map of the zone, based on the stream potential law (Hack, 1957), taking into account that $k_{int} < k_{volc}$. The areas with larger erosion coincide with zones of high SL values. So it is distinguishing, at least in this area, that more SL (surface uplift) means more erosion, therefore more SL means more bedrock uplift.

4. 5 Sinuosity index (SI)

30 Using the sinuosity of the mountain front, 7 segments were defined, whose SI values are summarized in Fig. 8. The result of segment 6 will not be considered in this analysis because the fault is located outside the piedmont in this segment, and thus the methodology is not valid there. Segments 1, 2 and 4 show values close to 1 (1.17 - 1.43), as observed in active reverse

faults (1.00-1.50) (Casa et al., 2010; Jain & Verma, 2006; Singh & Tandon, 2007; Wells et al., 1988). The specific segments where SI values are close to 1 also coincide with zones in which gravity profiles suggest fault activity. These segments have a mean value of 1.3, which reflects the limited capacity of the SRF to shape the mountain front, compared to the 1.04 mean value of the piedmont fault in the Himalayas (Jain & Verma, 2006). Segments 3, 5, 6, and 7 have higher SI values (>2).

5 **Fluctuating SI values indicate the occurrence of different geomorphologic processes dominating the fault scarp at the surface.**

4.6 Magnitude of the characteristic earthquake

The seismic moment magnitude M_w (Eq. 1 from Hank & Kanamori 1979), can be estimated geologically by the product of the crustal rigidity (μ), fault slip (S), and the fault area (L×W) (Eq. 2, Aki & Richards 1980).

10
$$M_w = \frac{2}{3}[\log(M_o) - 9.1], \quad (1)$$

$$M_o = \mu LWS, \quad (2)$$

In this work crustal rigidity is approximated by 3×10^{10} N m⁻²; fault width is estimated in 10-15 km based on the observed seismicity; and the average slip has been estimated in the range of 1 - 4 m (Armijo et al. 2010) or using the identified events in the paleoseismological study 4.8 ± 0.6 m (Vargas et al. 2014). In this work we assume a rather upper bound figure of average slip of 4 m. Regarding the rupture length, gravity modeling, stream gradient index, and the sinuosity results, allow the definition of 4 fault segments (shown in Fig. 9) that probably would become active independently, as we will discuss in section 5.3. These results also suggest a likely fault extension to the north of the study area, but not southward, at least as a piedmont fault. According to these considerations, the expected magnitude for the characteristic earthquake in any segment would be in the range of 6.2 - 6.7 M_w .

20 **4.7 Empirical model Chiou & Youngs results**

The results shown in Fig. 10a represent the maximum expected PGA in the study area. At each point we choose the largest PGA value from the corresponding rupture of every SRF sub-fault. Against intuition, the largest acceleration in the northern segment is observed in the footwall block instead of the hanging wall. This can be explained by the infilling of fine sediments (low shear velocity) with larger site effects compared to the basement rocks at the hanging wall. In the other segments to the south, as expected, the largest PGA is observed in the hanging wall. In segments 2 and 4 part of the hanging walls are filled with sediments, generating hanging wall and site effects with PGA values above 0.5g. The largest acceleration of 0.8g shows up in the area already described.

5. Discussion

5.1 Present-day fault activity

Seismic events spatially associated with the SRF, suggest that the fault is active. If this inference is correct, their depth distribution shows more affinity with a high angle fault (Fig. 3). This is consistent with the surface expression of the SRF as described by the Calán outcrop and the TEM profile (Fig. 4). Although reverse fault optimal orientation is low angle, several examples of normal high angle faults reactivated as inverse faults have been described in the Andean orogenesis (e.g. Charrier et al. 2002). Another aspect is the importance of the SRF on the whole stress release of the zone in terms of the seismic productivity. The natural seismicity distribution in the study area indicates that just five events can be related to SRF, representing 12% of the 41 well localized events, and 5% of all 110 crustal events regardless of their location error (but still within the area of interest). **This denotes that the San Ramón fault is not necessarily the most important structure in the deforming cordillera.** But, nevertheless it involves a significant hazard given its likely active condition and its proximity to the city.

5.2 Fault geometry, dip and depth of rupture

To simulate the acceleration is necessary to determine some fault first order geometrical characteristics. Fault type is the first one, that can generate a 0.8 factor to the acceleration for normal faults, and 1.3 for reverse ones, with respect to strike slip faults (Ambraseys et al. 2005). The TEM profile and the tilting strata in the Calán hill outcrop clearly demonstrate the reverse kinematics, also well supported by many field observations (Armijo et al., 2010; Rauld, 2011; Vargas et al., 2014). Another relevant variable is the shallow depth of the rupture (Youngs et al. 1997; Chiou & Youngs 2008). In SRF case, the quaternary sediments in the Calán hill are cut by the fault. Consistent with this observation, TEM results indicate that basement displacement is also reaching the basement roof (Fig. 4), and thus, breaking the surface. Therefore, the shallow depth of rupture is estimated at zero level. The last first order variable is the fault dip. The NGA-West 2 data indicates a systematical acceleration increasing with larger dips (Chiou & Youngs, 2014). The TEM profile and the Calán outcrop show a near-surface subvertical plane. **At depth, the micro-seismic study is also consistent with a high angle fault; therefore the dip angle of SRF is estimated at 65 degrees.**

5.3 FSR segmentation

According to the integrated analysis carried out the SRF is not necessarily a continuous fault along its ~30 km of NS extension, but rather a segmented one. In this section we discuss the most likely fault configuration. Locations of fault segments are included in Fig. 9.

The northern segment (section 1 in Fig. 9), is not necessarily restricted to the length defined in this work because with the information available we cannot trace precise limits. Mainly because the gravity profiles are a bit sparse. Nevertheless the

existence of the fault in this zone is demonstrated by the stream gradient signal and the gravity profile L2. Despite this drawback, we postulate this segment as a preliminary solution.

In the central area, we propose three segments capable to generate a great earthquake (segments 2, 3 and 4 Fig. 9), with a high uplift interpreted by the high values of SL, and the surface manifestation of the SRF (Armijo et al., 2010; Rauld, 2011).

5 The segmentation of sections 2 and 4 is supported by the gravity profile and the fluctuant sinuosity index, complemented by lithological changes in the hanging wall unit (Fig. 8). In fact, the transition zone between segments 2 and 3 is supported by the lack of gravity signal in two adjacent profiles (L9 and L10). In addition, the sinuosity index value of 2.33 in this transition zone is much greater than the expected values for active faults. Finally, we observed lower – middle Pleistocene fluvial and alluvial sediments on the hanging wall of segment 2, whereas these deposits disappear southward in segment 3.

10 In segment 3 the hanging wall deposits are middle - upper Pleistocene sediments. This suggests a larger uplift activity on segment 2, capable to preserve older coverage.

To the south, the separation of the segments 3 and 4 is mainly argued on the longitude discontinuity of the fault scarps observed on the surface, and on the gravity-derived basement morphology. An example of this discontinuity is represented by the intrusion of the Miocene La Obra granite (Fig. 8). This more competent unit may be responsible for the offset in the

15 rupture plane.

Based on the arguments listed previously our first order approximation states that segments 2, 3 and 4 behave as independent ruptures, where each one can generate a similar characteristic earthquake.

An important discussion is how independent could be the rupture of segments 2, 3 and 4, which are separated by less than 3km. In this scenario it has been suggested that the activation of one segment can trigger the displacement of the adjacent

20 segment (Wesnousky, 2008). However, this behavior is evident in 60% of the cases in strike slip faults, but not necessarily applicable to reverse faults (Wesnousky, 2008). Some examples of continuous ruptures associated with a specific earthquake are Chi-Chi 1999, Taiwan (Chen et al., 2001), Marryat Creek 1986, Australia (Machette, Crone, & Bowman, 1993) the Mikawa 1945 earthquake, Japan (Wesnousky, 2008), and the Asnam 1980, Argelia (Yielding et al., 1981). In the last case segmented ruptures are formed, but are produced by several events.

25 In order to discuss the potential activation of several SRF segments, we propose possible scenarios. One possibility is the triggering of a segment given the displacement in the adjacent segment. This case does not imply more hazard because these events are not simultaneous. Another possibility is that at deeper levels the SRF behaves as a single unit, but their stress releases are discontinuous in space at the surface. One example of such a behavior in reverse faults has been observed at Tennat Creek earthquake. During this earthquake a single event generated a discontinuous rupture at surface (Crone, Machette, & Bowman, 1989).

30 According to Crone et al. (1989), this discontinuity was produced by the existence of an along-strike rupture barrier. Until now there is no geological evidence in SRF of a rupture barrier as the one identified in the Tennant Creek case. At this regard, our results suggest that deformation is accommodated in several faults that reach the surface. In fact, gravity profiles (Fig. 6) and TEM imaging (Fig. 4) demonstrate the presence of several faults cutting the upper level of the basement. The observed near surface displacement has been estimated by means of the time-integration

(since at least 100 Kyr) methodologies: gravity modeling and sinuosity index. These observations are not consistent with a continuous and homogeneous displacement along the whole fault trace in a time window (> 100 Kyr) that must involve the occurrence of several characteristic earthquakes.

Although we cannot rule out a single rupture of the whole FSR segments, our evidences consistently favor the occurrence of a single segment characteristic earthquake, with a rupture length of ~ 10 km.

5.4 Seismic hazard zoning

Based on the characteristic earthquake definition, we present the PGA response associated with the SRF in Fig. 10 (described in detail in section 4.7). To determine the expected damage we need appropriate fragility curves for the study zone and the corresponding building typology, which are not available. Alternatively, we have the chance to compare the expected acceleration with the reported effects of the Maule 2010 earthquake ($M_w = 8.8$). This megathrust event generated 0.56g of PGA in a district of the city with a low shear velocity (Barrientos, 2010). The acceleration of the Maule event, and the expected in SRF are both shown in Fig. 10. Accelerometers that recorded the largest PGA values during the Maule 2010 earthquake coincide with reported damages in homes and building collapses nearby. Equivalent damages are observed in the northern Santiago district, where site effects associated with low shear wave velocity soils induced large PGA responses. However in this case, instrumental acceleration records are not available. Despite the scarce data support, we assume a deterministic approach, where 0.56g PGA can cause construction collapsing. Under the assumption of a fault displacement, segments of the hanging walls side of the SRF filled with sediments have an extreme high risk (PGA in the range of 0.5g to 0.8g). In Chile the construction norm does not ponder the existence of crustal faults, and the PGA estimated to building design for Santiago city is 0.3g, based only on the occurrence of subduction earthquakes without site effects. This acceleration estimate is fulfilled in the majority of the subduction earthquakes. The Maule 2010 earthquake effects represent a good example of such a behavior (Fig. 10), and consequently, the associated building damage in 0.3g-zones were minor. Therefore, the sectors of the Santiago basin with expected acceleration higher than 0.3g in San Ramón PGA map, involve a moderate risk. Finally, the possible surface rupture of the SRF implies the highest collapse risk because the constructions are made to resist no more than 1% of differential settlements. That means, at most 0.5 meters in a 50-meters-width building. This number is widely exceeded by the expected 1 - 4 meter of average slip. In addition, TEM and gravity evidences suggest that surface ruptures are not always breaking the surface at the same place (Fig. 4 and 5). Therefore the possible surface rupture zone is an area, and not the mapped fault-trace line in surface.

The extremely high risk zones of the area (hanging wall filled with sediments) are located to the east of segments 2 and 4 (Fig. 10). The hanging wall of segment 2 is almost completely urbanized now, mainly with houses of one or two floors, with better resistance than the buildings, given their larger rigidity. The other extremely high risk zone on hanging wall of segment 4 has few constructions, and until 2015 is mostly a low-density urbanized zone. Given this scenario, a successful mitigation measure must limit the buildings construction in these areas, or at least not allowing the unreinforced masonry buildings. In addition, the norm must prohibit building in the proximity of the surface rupture, with special emphasis on

public buildings like hospital or schools, and industrial buildings that may cause major damage, such as gas stations or nuclear research plants.

6. Conclusion

Natural seismicity registered in a one-year local network is compatible with SRF activity. However, stress release as seismic activity along the SRF is secondary compared to the activity observed in other sectors near Santiago city.

Geophysical and geomorphological evidences suggest that the SRF is segmented into 4 sub-faults that most likely are activated independently. Under this scenario a characteristic earthquake of magnitude $M_w = 6.2 - 6.7$ is expected.

Based on the TEM imaging, Calán Hill outcrops, and seismic evidences the SRF is a high angle structure. This geometry is also supported by surface scarp expression and by the basement scarp geometry derived from the gravity modeling.

If SRF is activated, it can produce building collapse, therefore it is necessary to take preventing actions to avoid catastrophic damages. In particular, construction in the rupture zone must be highly restricted, as well as limiting the unforced masonry buildings in hanging walls filled with sediments.

The integrated methodology applied in this study provides a valuable tool to estimate the seismic risk associated to crustal faults with low slip rate and subtle surface evidences.

15 Acknowledgments

We want to thank the important field support provided by A. Mella, A. Bosh, N. Moraga, G. Sielfeld, I. Santibañez, B. Perez, S. Pérez, R. Figueroa, M. Lizama. T. García kindly provided field support as well as her expertise in geophysical software. We thank G. Cassasa and A. Yañez for providing their homes to install a seismic station over a year, and ENERGÍA ANDINA for providing their seismometers. CG5 gravimeter was provided by CEGA, FONDAP-CONICYT project N°15090013. TEM experiment was partially supported by Fondecyt project N° 1141139. DICTUC S.A and CIGIDEN (FONDAP-CONICYT project N°15110017) provided economic support for the development of this work. Last but not least, we appreciate the discussions with G. Arancibia, J. Cembrano, T. Roquer and all the emerging Geosciences group at PUC.

25 Reference

Aki, K., & Richards, P. G.: *Quantitative Seismology: Theory and Methods*. New York: W. H. Freeman, 1980.

Ambraseys, N. N., Douglas, J., Sarma, S. K., & Smit, P. M.: Equations for the estimation of strong ground motions from shallow crustal earthquakes using data from Europe and the middle east: Horizontal peak ground acceleration and spectral

- acceleration. *Bulletin of Earthquake Engineering*, 3(1), 1–53, 2005.
- Armijo, R., Rauld, R., Thiele, R., Vargas, G., Campos, J., Lacassin, R., & Kausel, E.: The West Andean Thrust, the San Ramón Fault, and the seismic hazard for Santiago, Chile. *Tectonics*, 29(2), TC2007, 1–34, 2010.
- Barrientos, S. E.: Terremoto (M=8.8) del 27 de febrero de 2010 en Chile. *Revista de La Asociación Geológica Argentina*, 5 67(3), 412–420, 2010.
- Blaser, L., Kruger, F., Ohrnberger, M., & Scherbaum, F.: Scaling Relations of Earthquake Source Parameter Estimates with Special Focus on Subduction Environment. *Bulletin of the Seismological Society of America*, 100(6), 2914–2926, 2010.
- Bull, W. B., & McFadden, L. D.: Tectonic geomorphology north and south of the Garlock fault, California. *Doehring, D.O. Ed. Geomorphology in Arid Regions: Binghamton*, 115–138, 1977.
- 10 Carretier, S., Ritz, J. F., Jackson, J., & Bayasgalan, A.: Morphological dating of cumulative reverse fault scarps: Examples from the Gurvan Bogd fault system, Mongolia. *Geophysical Journal International*, 148(2), 256–277, 2002.
- Casa, A. L., Cortés, J. M., & Borgnia, M. M.: Pleistocene evidences of deformation in the La Carrera fault system (32°40'–33°15'LS), Cordillera Frontal of Mendoza. *Revista de La Asociación Geológica Argentina*, 67(1), 91–104, 2010.
- Charrier, R., Baeza, O., Elgueta, S., Flynn, J. J., Gans, P., Kay, S. M., Muñoz, N., Wyss, A. R., Zurita, E.: Evidence for 15 Cenozoic extensional basin development and tectonic inversion south of the flat-slab segment, southern Central Andes, Chile (33°–36°S.L.). *Journal of South American Earth Sciences*, 15(1), 117–139, 2002.
- Chen, Y.-G., Chen, W.-S., Lee, J.-C., Lee, Y.-H., Lee, C.-T., Chang, H.-C., & Lo, C.-H.: Surface rupture of 1999 Chi-Chi earthquake yields insights on active tectonics of central Taiwan. *Bulletin of the Seismological Society of America*, 91(5), 977–985, 2001.
- 20 Chiou, B. S. J., & Youngs, R. R.: NGA Model for Average Horizontal Component of Peak Ground Motion and Response Spectra. *Pacific Engineering Research Center Report*, (November), 1–94, 2008.
- Chiou, B. S. J., & Youngs, R. R.: Update of the Chiou and Youngs NGA Ground Motion Model for Average Horizontal Component of Peak Ground Motion and Response Spectra. *Earthquake Spectra*, 30(August), 1117–1153, 2014.
- Crone, A. ., Machette, M. ., & Bowman, J. R.: *Geologic investigations of the 1988 Tennant Creek, Australia, Earthquakes - 25 Implications for Paleoseismicity in Stable Continental Regions*. (U. S. geological Survey, Ed.). Washington: United States government printing office, 1989.
- Díaz, D., Maksymowicz, A., Vargas, G., Vera, E., Contreras-Reyes, E., & Rebolledo, S.: Exploring the shallow structure of

- the San Ramón thrust fault in Santiago, Chile (~33.5° S), using active seismic and electric methods. *Solid Earth*, 5(2), 837–849, 2014.
- Farías, M., Charrier, R., Carretier, S., Martinod, J., Fock, A., Campbell, D., Cáceres, J., Comte, D.: Late Miocene high and rapid surface uplift and its erosional response in the Andes of central Chile (33°-35°S). *Tectonics*, 27(1), TC1005, 1–22, 5 2008.
- Fernández, J. C.: Repuesta sísmica de la cuenca de Santiago, Región Metropolitana de Santiago. *Carta Geológica de Chile: Serie Geología Ambiental*, 2003.
- Font, M., Amorese, D., & Lagarde, J.-L.: DEM and GIS analysis of the stream gradient index to evaluate effects of tectonics: The Normandy intraplate area (NW France). *Geomorphology*, 119(3-4), 172–180, 2010.
- 10 Godoy, E., Yañez, G., & Vera, E.: Inversion of an Oligocene volcano-tectonic basin and uplift of its superimposed Miocene magmatic arc, Chilean central Andes: First seismic and gravity evidence. *Tectonophysics*, 306, 217–236, 1999.
- Hack, J. T.: Studies of Longitudinal Stream Profiles in Virginia and Maryland, U.S. *Geological Survey Professional Paper 294-B*, p. 97, 1957.
- Hack, J. T.: Stream-profile analysis and stream-gradient index. *Journal of Research of the US Geological Survey*. 1(4), 421 – 15 429, 1973.
- Hank, T. C., & Kanamori, H.: A Moment Magnitude Scale. *Journal of Geophysical Research*, 84, 2348–2350, 1979.
- Jain, S., & Verma, P. K.: Mapping of active tectonics intensity zones using remote sensing and GIS. *Journal of the Indian Society of Remote Sensing*, 34(2), 131–142, 2006.
- Kurtz, A. C., Kay, S. M., Charrier, R., & Farrar, E.: Geochronology of Miocene plutons and exhumation history of the El 20 Teniente region, central Chile (34°-35°S). *Revista Geológica de Chile*, 24(1), 75–90, 1997.
- Leyton, F.: Zonificación sísmica de la cuenca de santiago, chile. *X Congreso Chileno de Sismología E Ingeniería Antisísmica*, Antofagasta, Chile, 2010.
- Machette, M., Crone, A., & Bowman, R. J.: Geologic investigations of the 1986 Marryat Creek, Australia, earthquake: implications for paleoseismicity in stable continental regions. *USGS Bulletin, Report B 2*, B1–B28, 1993.
- 25 Merritts, D., & Vincent, K. R.: Geomorphic response of coastal streams to low, intermediate, and high rates of uplift, Mendocino triple junction region, northern California. *Geological Society of America Bulletin*, 101, 1373–1388, 1989.

- Moore, J. R., Sanders, J. W., Dietrich, W. E., & Glaser, S. D.: Influence of rock mass strength on the erosion rate of alpine cliffs. *Earth Surface Processes and Landforms*, 34, 16–25, 2009.
- Mpodozis, C., & Ramos, V. (1989). The Andes of Chile and Argentina. *Geology of the Andes and Its Relation to Hydrocarbon and Mineral Resources*, 11, 59–90, 1989.
- 5 Pérez, A., Ruiz, J., Vargas, G., Rauld, R., Rebolledo, S., & Campos, J.: Improving seismotectonics and seismic hazard assessment along the San Ramón Fault at the eastern border of Santiago city, Chile. *Natural Hazards*, 71(1), 243–274, 2014.
- Rauld, R.: *Deformación cortical y peligro sísmico asociado a la falla San Ramón en el frente cordillerano de Santiago, Chile Central (33°S)*. Ph.D. thesis. Universidad de Chile, 2010.
- Rauld, R., Vargas, G., Armijo, R., Ormeño, A., Valderas, C., & Campos, J.: Cuantificación de escarpes de falla y deformación reciente en el frente cordillerano de Santiago. In *X Congreso Geológico Chileno*. Antofagasta, Chile, 2006.
- 10 Sadigh, K., Chang, C.-Y., Egan, J. A., Makdisi, F., & Youngs, R. R.: Attenuation Relationships for Shallow Crustal Earthquakes Based on California Strong Motion Data. *Seismological Research Letters*, 68(1), 180–189, 1997.
- Scawthorn, C., & Rathje, E. M.: The 2004 Niigata Ken Chuetsu, Japan, Earthquake. *Earthquake Spectra*, 22(S1), 1–8, 2006.
- Schwartz, D. P., & Coppersmith, K. J.: Fault behavior and characteristic earthquakes - examples from the Wasatch and San-
15 Andreas fault zones. *Journal of Geophysical Research*, 89(NB7), 5681–5698, 1984.
- Singh, V., & Tandon, S. K.: Evidence and consequences of tilting of two alluvial fans in the Pinjaur dun, Northwestern Himalayan Foothills. *Quaternary International*, 159, 21–31, 2007.
- Stern, C., Amini, H., Charrier, R., Godoy, E., Hervé, F., & Varela, J.: Petrochemistry and age of rhyolitic pyroclastic flows which occur along the drainage valleys of the Río Cachapoal (Chile) and the Río Yaucha and Río Papagayos (Argentina).
20 *Revista Geológica de Chile*, 23, 39–52, 1984.
- Stock, J. D., & Montgomery, D. R.: Geologic constraints on bedrock river incision using the stream power law. *Journal of Geophysical Research*, 104(B3), 4983–4993, 1999.
- Telford, W. M., Geldart, L. P., & Sheriff, R. E.: Applied Geophysics. *Cambridge University Press*, UK, 1990.
- Thiele, R.: Hoja de Santiago, Región Metropolitana. *Carta Geológica de Chile*, 39, 51, 1980.**
- 25 Vargas, G., Klinger, Y., Rockwell, T. K., Forman, S. L., Rebolledo, S., Baize, S., Lacassin, R., Armijo, R.: Probing large intraplate earthquakes at the west flank of the Andes. *Geology*, 42(12), 1083–1086, 2014.

Villegas, L.: *Estructura sísmica cortical en los andes centrales (33°-34.5°s): concentraciones de sismicidad bajo minas el teniente y disputada. Ph.D. thesis. Universidad de Chile, 2012.*

Wells, Bullard, T. F., Menges, C. M., P.G., D., Karas, P. A., Kelson, K. I., Ritter, J. B., Wesling, J.: Regional variations in tectonic geomorphology along a segmented convergent plate boundary, Pacific coast of Costa Rica. *Geomorphology*, 1, 239–265, 1988.

Wells, D. L., & Coppersmith, K. J.: New Empirical Relationships among Magnitude, Rupture Length, Rupture Width, Rupture Area, and Surface Displacement. *Bulletin of the Seismological Society of America*, 84(4), 974–1002, 1994.

Wesnousky, S. G.: Displacement and geometrical characteristics of earthquake surface ruptures: Issues and implications for seismic-hazard analysis and the process of earthquake rupture. *Bulletin of the Seismological Society of America*, 98(4), 1609–1632, 2008.

Yañez, G., Muñoz, M., Flores-Aqueveque, V., & Bosch, A.: Gravity derived depth to basement in Santiago Basin, Chile: implications for its geological evolution, hydrogeology, low enthalpy geothermal, soil characterization and geo-hazards. *Andean Geology*, 42 (2), 147–172, 2015.

Yielding, G., Jackson, J. a., King, G. C. P., Sinvhal, H., Vita-Finzi, C., & Wood, R. M.: Relations between surface deformation, fault geometry, seismicity, and rupture characteristics during the El Asnam (Algeria) earthquake of 10 October 1980. *Earth and Planetary Science Letters*, 56, 287–304, 1981.

Youngs, R. R., Chiou, S.-J., Silva, W. J., & Humphrey, J. R.: Strong Ground Motion Attenuation Relationships for Subduction Zone Earthquakes. *Seismological Research Letters*, 68(1), 58–73, 1997.

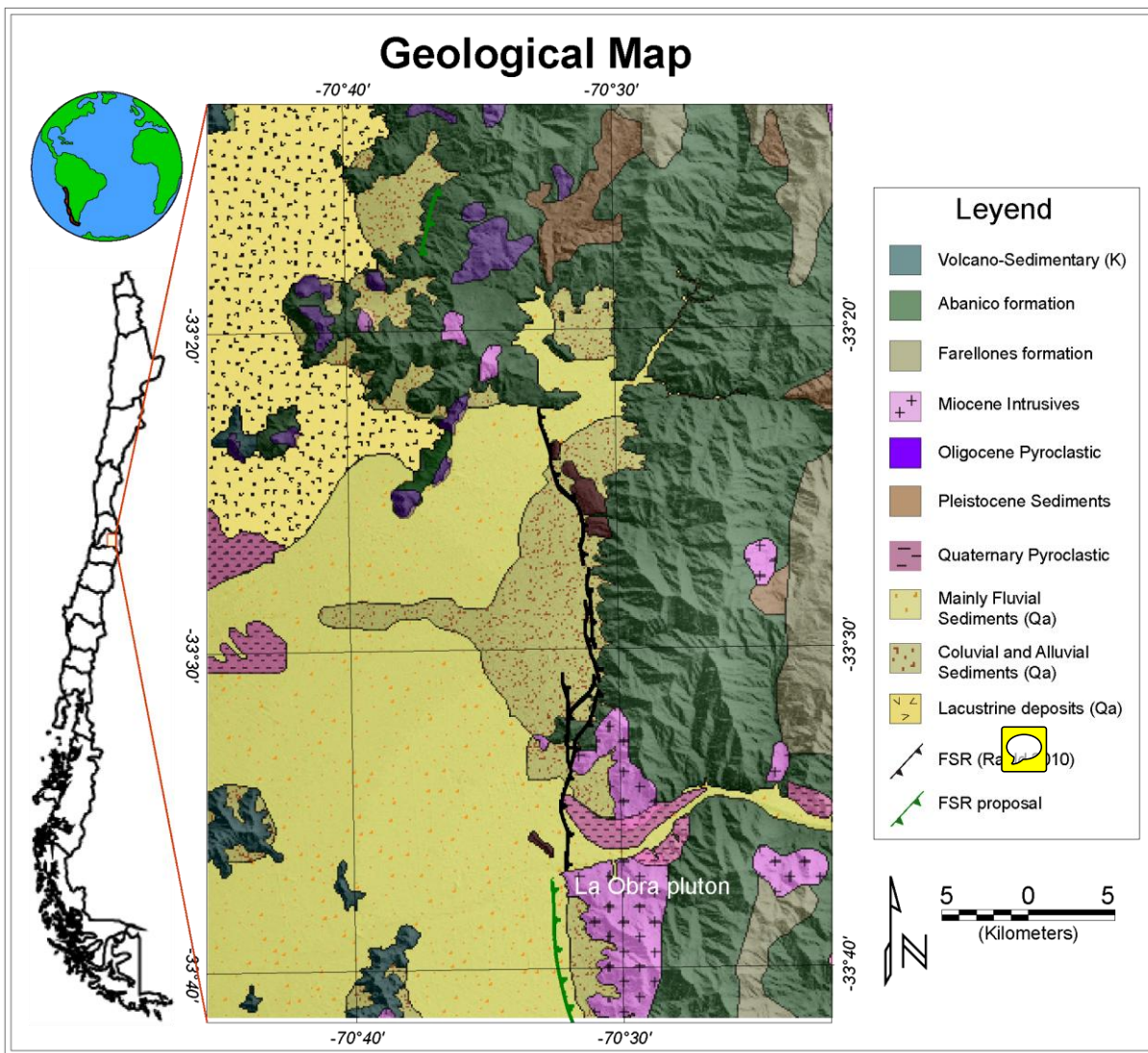


Figure 1. Geological map of the zone (Thiele 1980; Fernández 2003).

5

10

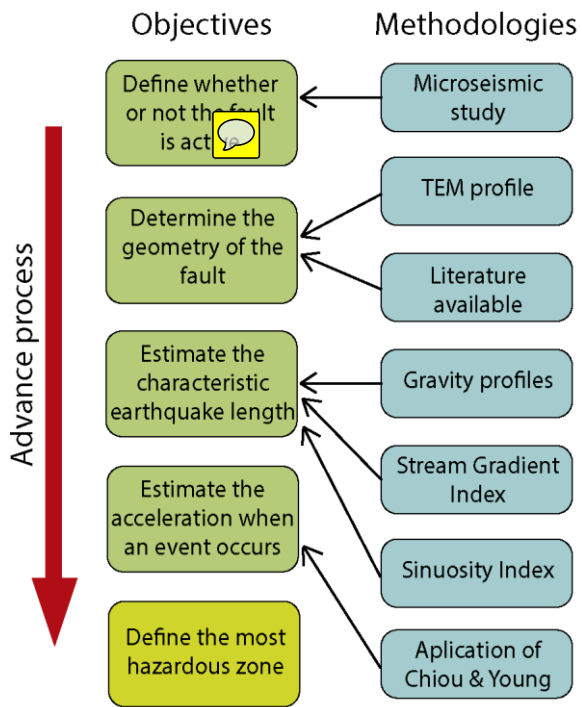


Figure 2. Scheme of objectives and methodologies used in this work. In yellow the final objective.

5

10

15

Micro-seismic study result

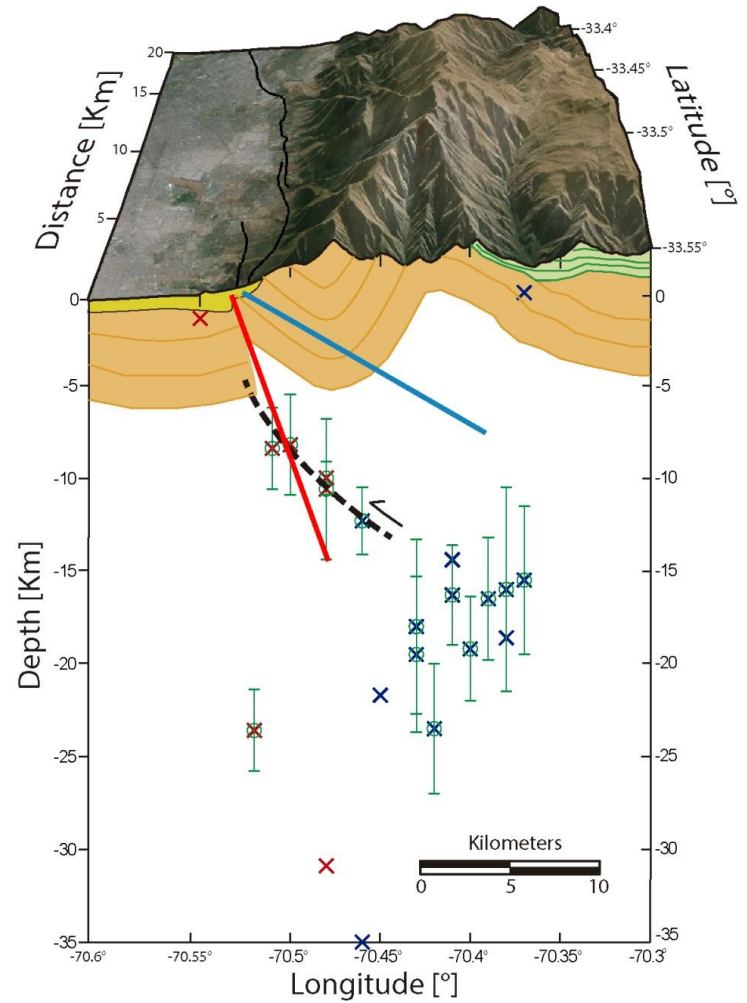
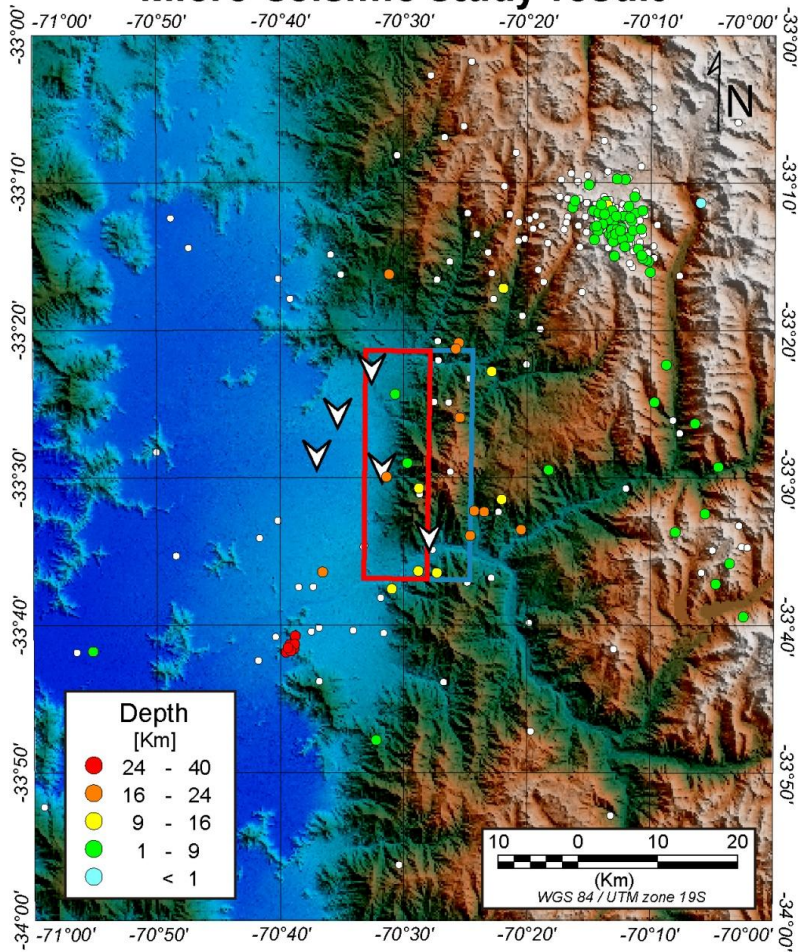
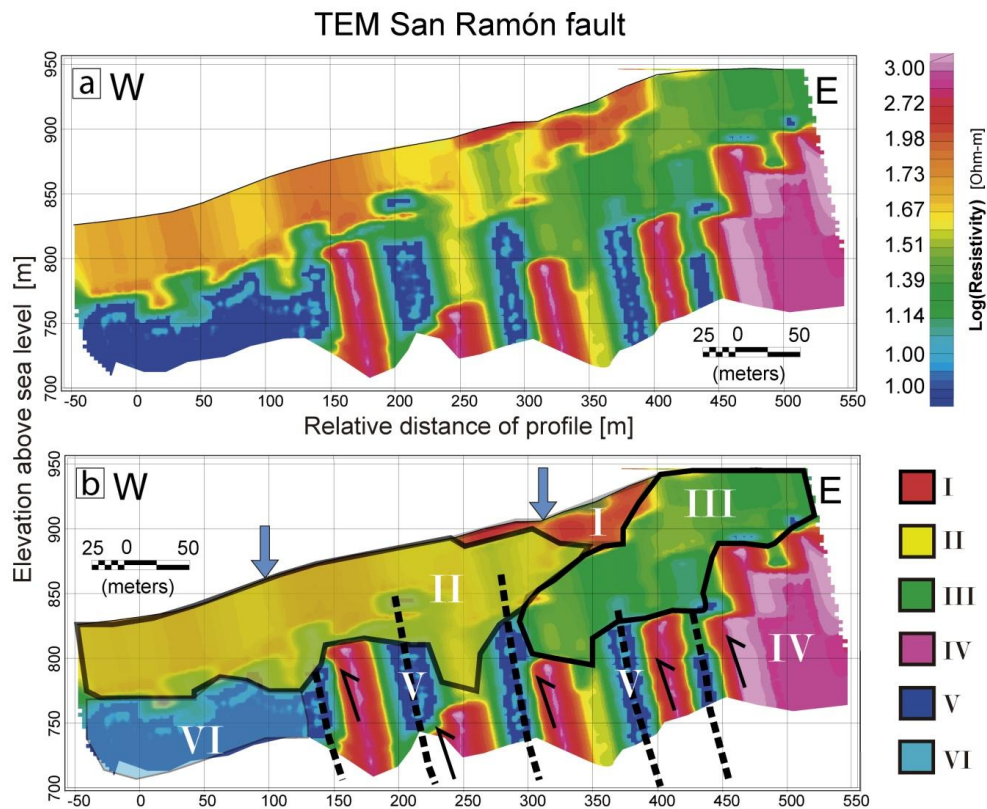


Figure 3. Microseismic study results. In the left panel, the map with epicenters of the recorded events, the color means depth of the hypocenter. In white the event with localization errors larger than 8km. The red rectangle represents the 70° projection plane on surface, and the blue rectangle the corresponding 30° projected plane. The right panel shows the seismic profile with well recorded events (depth error bands in green). The poorly localized events are indicated without error bars. The red and blue lines represent the planes of 70° and 30° respectively. The dashed black line represents the interpretation of the SRF.





Outcrop of SRF in Calán hill

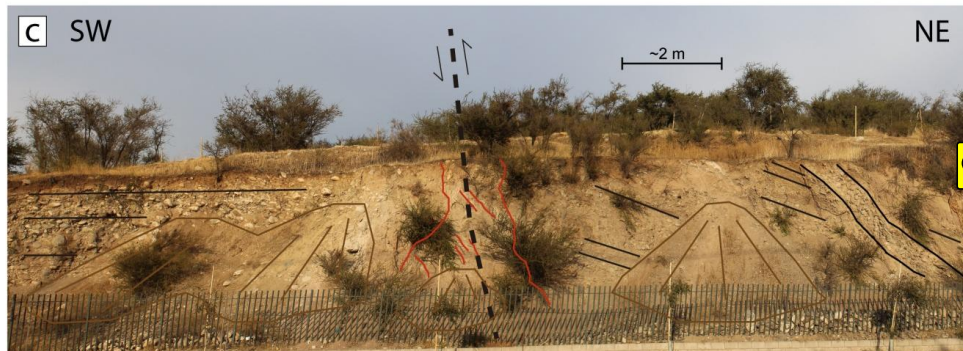


Figure 4. TEM results and the Calán hill outcrop. a) TEM inversion results. b) Interpretation of the TEM profile, the blue arrow indicates the fault scarp in surface, and the roman numbers are the different lithologic units identified. c) Calán hill outcrop, in this section we can observe the tilting against the natural slope of the sediments strata to the east. This tilting is produced by the SRF enclosed in red line, with kinematic represented by the dash line in black. The fault cuts quaternary sediments. At the SW side imbricated fluvial sediments show a horizontal stratification. In brown the colluvial formed by the breakdown clasts.

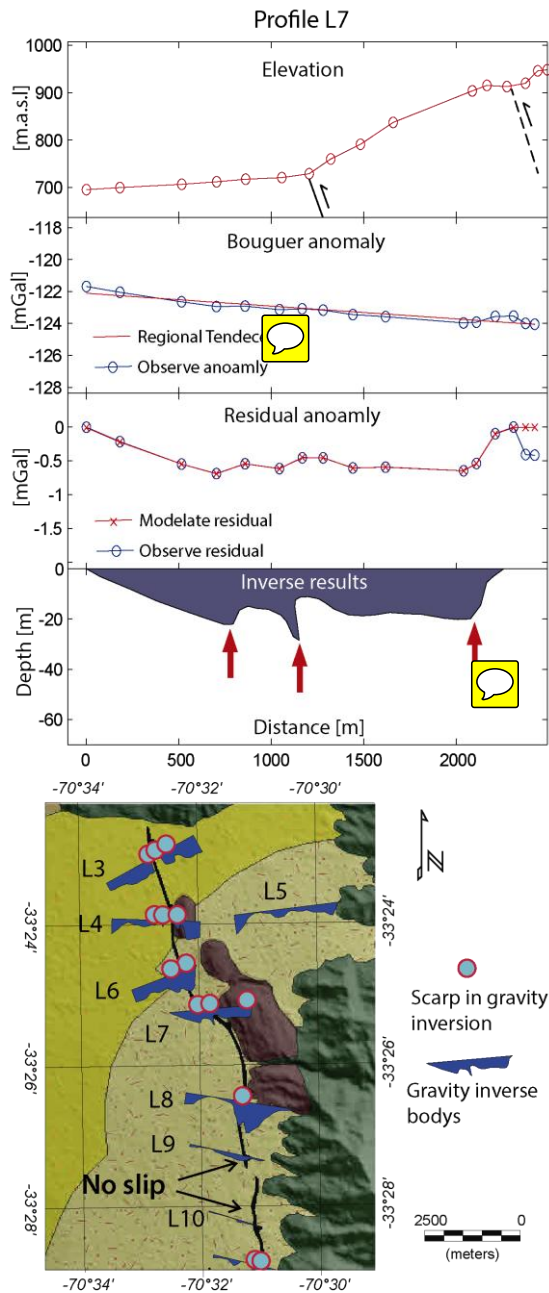


Figure 5. In the upper panel the results of gravity inversion of profile 7. In the elevation profile the observed surface scarp is drawn (Rauld 2011). The regional tendency is calculated by a first order approximation. In the inverse profile the red arrow shows the interpreted faults scarp. In the lower panel, the results of profiles 3 to 10 in planar view.

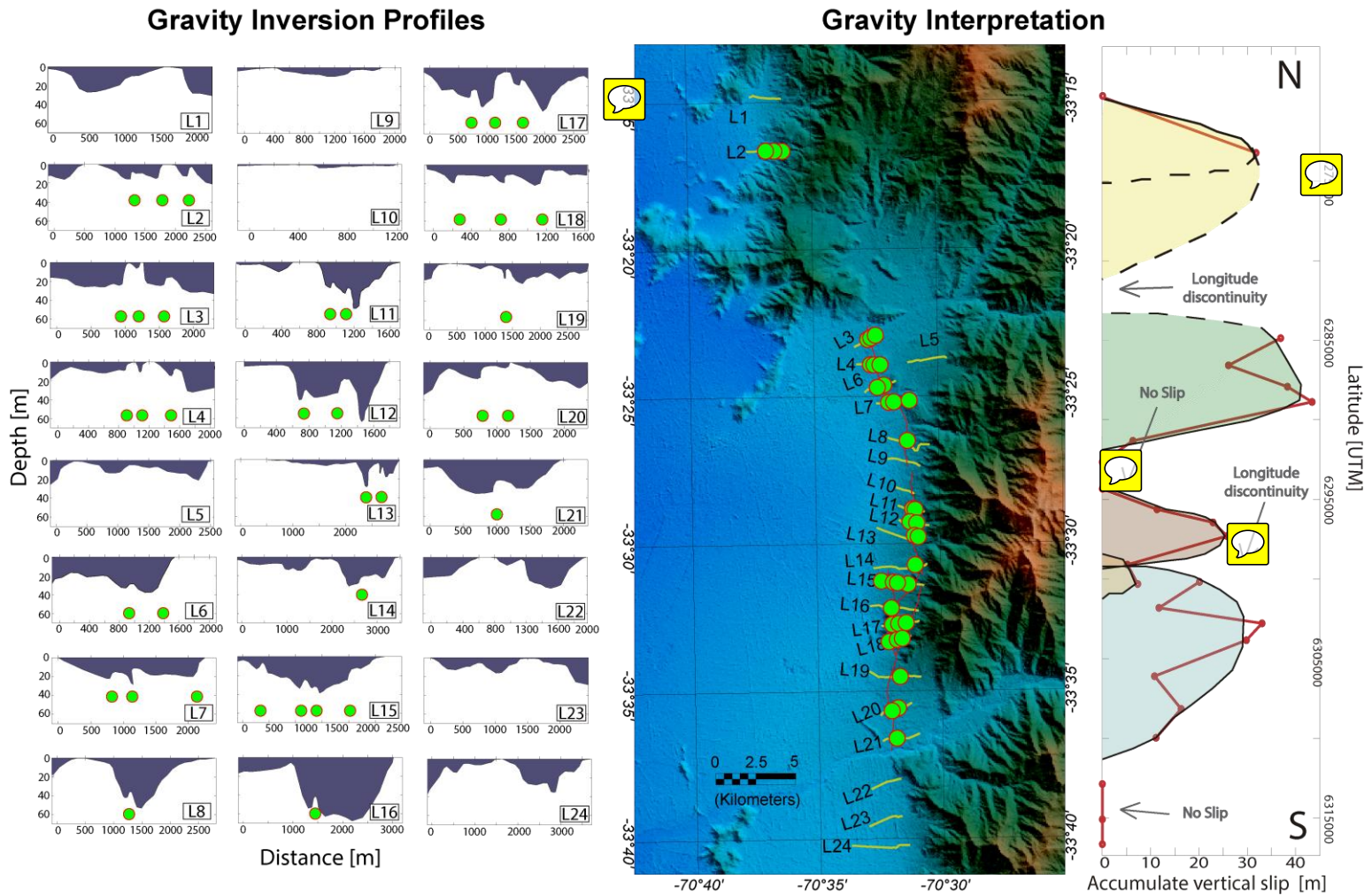


Figure 6. Gravity profiles results. In the left panel the gravity profiles inversion. The green points represent the observed basement scarp. In the middle panel the gravity results in planar view. **This view allows the fault continuity interpretation.** The right panel shows the slip accumulated in each profile in red line, and the interpreted fault segments in different colors.

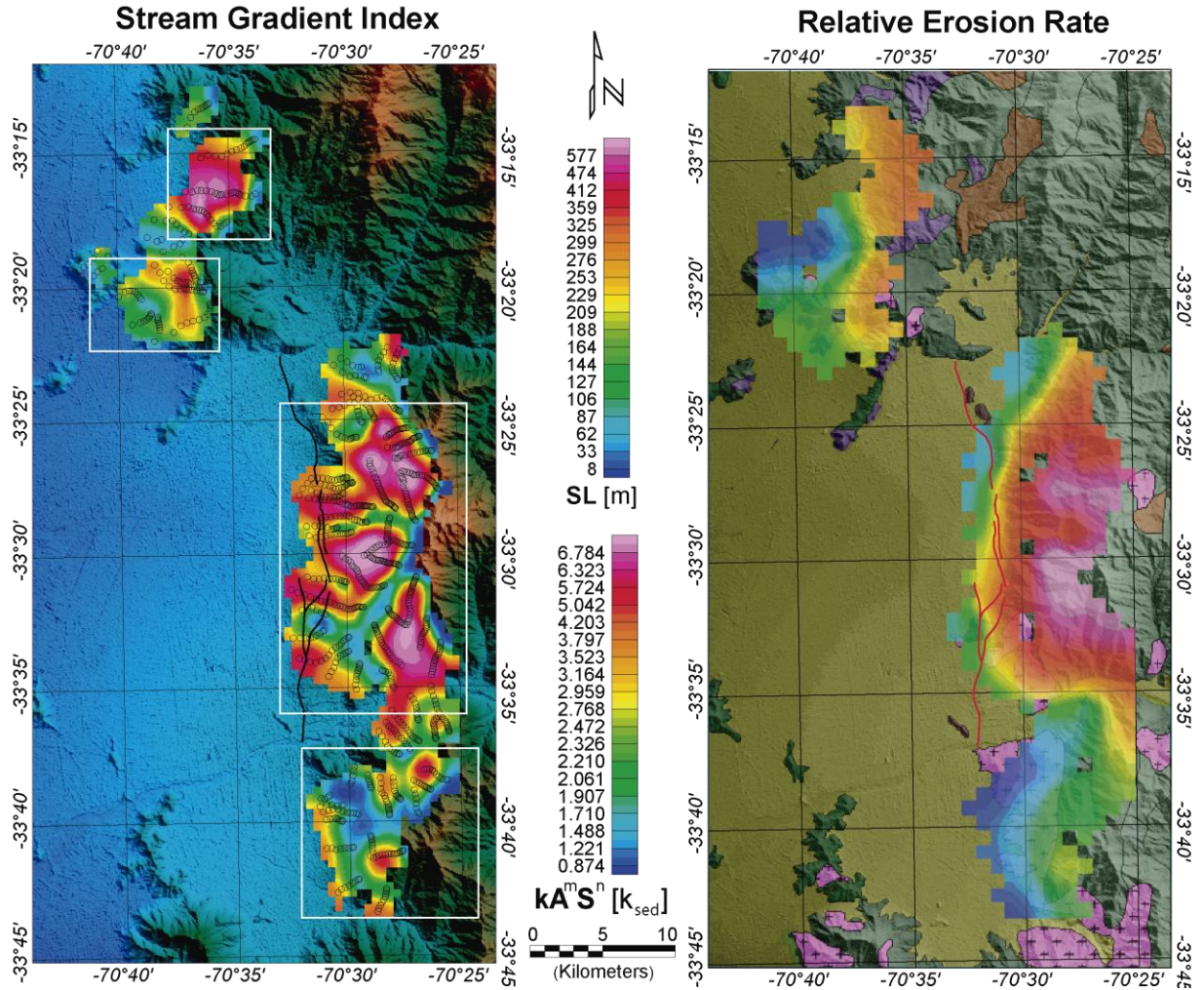


Figure 7. Stream gradient index and relative erosion representation. In the left panel we present the stream gradient index results, the points represent the middle of each segment where the SL is measured. In the right panel the relative erosion rates calculated for each drainage with $m=0.28$ $n=1$, and assuming that $k_{\text{sedimentary rock}} = 2 \times k_{\text{intrusive rock}}$. This map must be multiplied by $k_{\text{sedimentary rock}}$ to obtain absolute erosion rate values. $k_{\text{sedimentary rock}} > k_{\text{intrusive rock}}$ is demonstrated for the zone by the knickpoints related with the intrusive rock in the main rivers Maipo, Mapocho, and Aconcagua (Farías et al. 2008).

Sinuousity Index

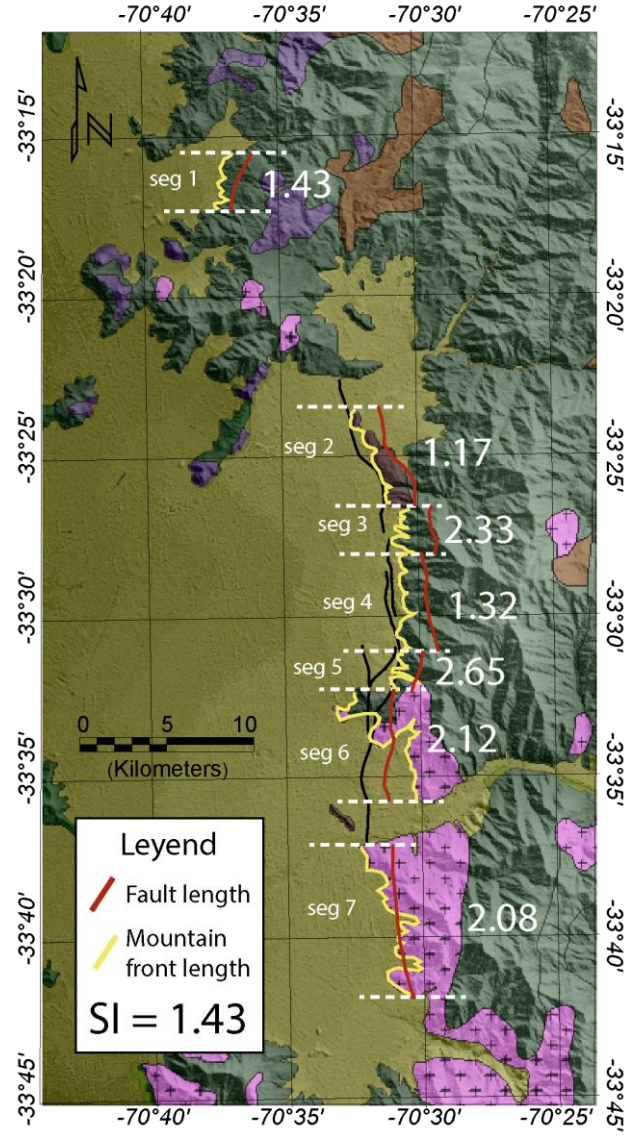


Figure 8. Sinuousity Index results, in white the SI values.

5

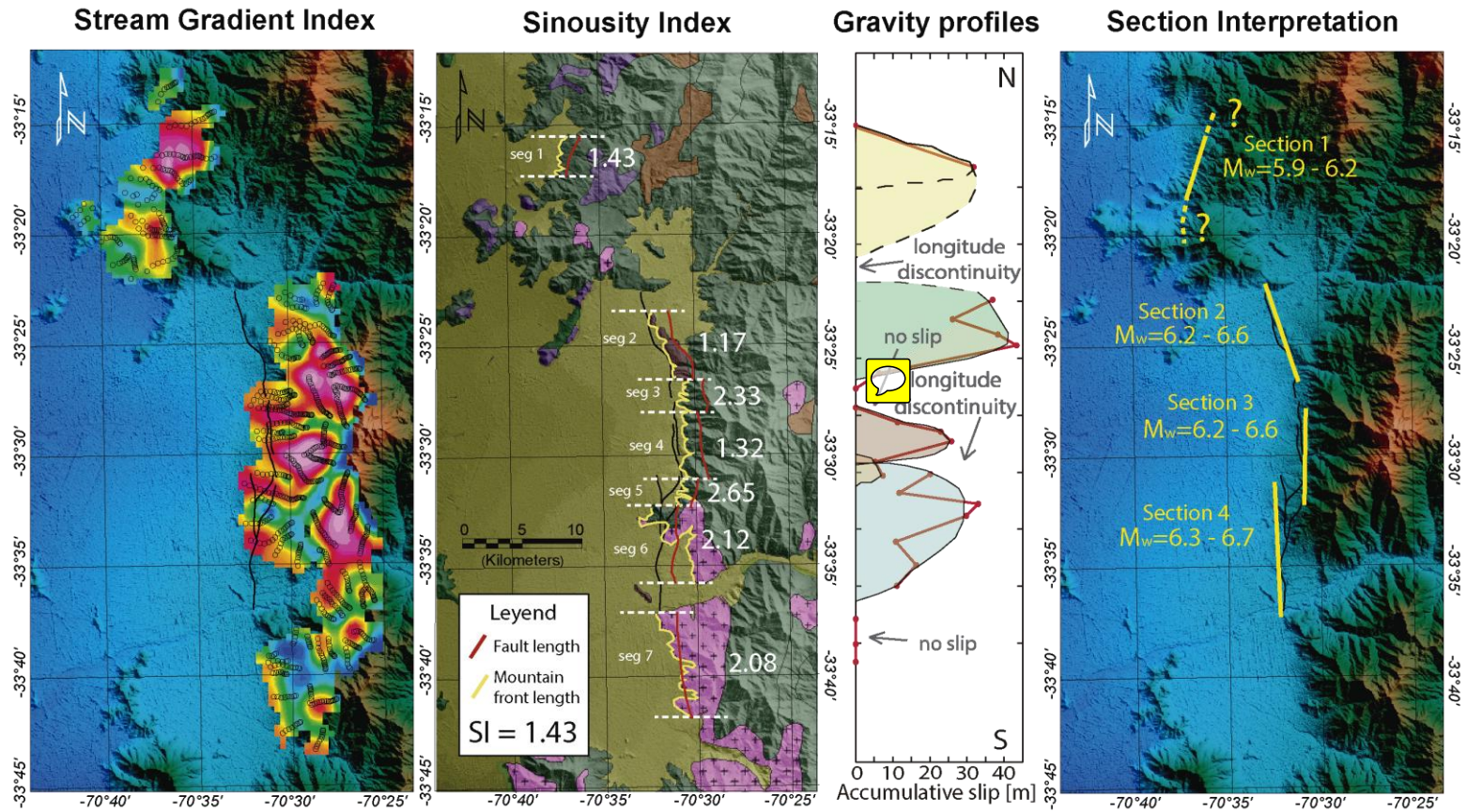


Figure 9. Interpretation of SRF sub-domains or sections. It summarizes the results of the 3 methodologies used to define the length of the characteristic earthquake, and the section interpretation. Section 1: the northern part has a high value of stream gradient index, additionally it has a low SI value and one gravity profile with ~30m of cumulative slip. Section 2: It is spatially related with the central area with high values of stream gradient index, also it has a low SI value and several basement scarps observed in gravity profiles (shown in Fig. 6) with a cumulative slip of 40m in mean. Section 3: separated from section 2 by high SI value, and without anomalies in two gravity profiles; it presents well developed surface scarps. Still located in the central high SL index area with a SI value close to 1, and several gravity profiles with basement scarp signature. Section 4: separated from section 3 by a longitude discontinuity, still located in the central high SL index area, and with several gravity profiles with basement scarp signature. The high value of the SI is interpreted by a section where this methodology is not applicable because the fault is not at the piedmont.

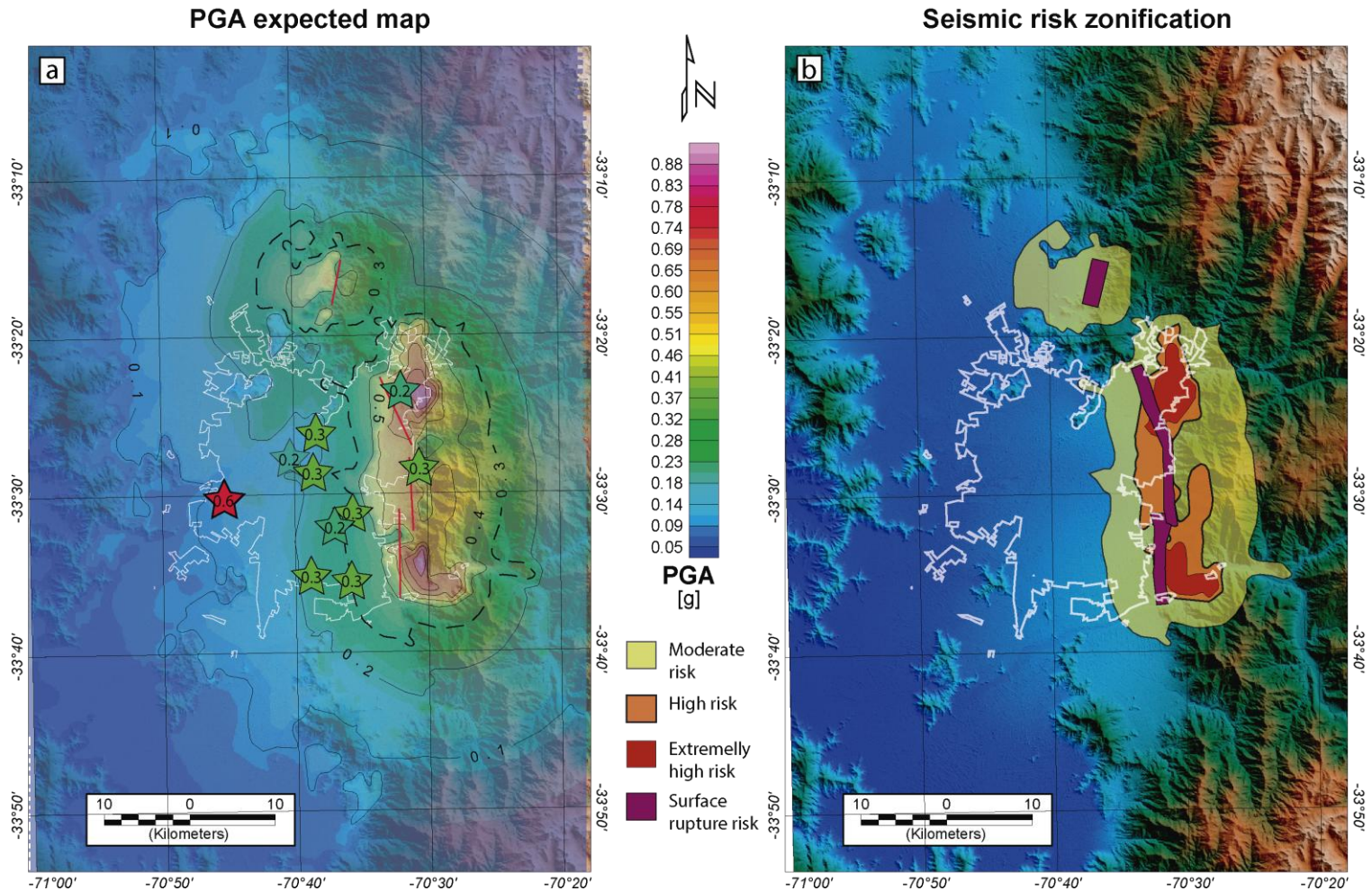


Figure 10. a) Expected PGA map of the largest acceleration of each point taking into account the 4 probable rupture scenarios. The stars represent the PGA recorded on the 2010 Maule event (Mw=8.8) (Barrientos 2010) in the same color scale. b) Seismic risk zoning: in yellow the area with acceleration greater than 0.3g which is the design PGA estimate by the Chilean norm. In orange the area with more than 0.4g. In red the hanging wall filled with sediments which concentrate the greatest PGA > 0.5g. In purple the zone with a possible surface rupture, based on the basement scarps identified in gravity profiles.